



POLITECNICO
MILANO 1863

Computational Fluid Dynamics
Dipartimento di Scienze e Tecnologie Aerospaziali
Politecnico di Milano

Design of a DRS rear wing

Marco Castelletti 10565826
Alessandro Celli 10615969
Lorenzo Fossati 10581461
Riccardo Gaudioso 10570792
Giovanni Girardello 10634962

Prof. Alberto Matteo Attilio Guardone
Tutor: Luca Abergó

Contents

1	Summary	1
2	Problem definition	2
2.1	Literature review	2
3	Design of Experiment	4
4	Computational model	5
4.1	Problem geometry and setup	5
4.1.1	Geometry definition	5
4.1.2	Boundary conditions	6
4.2	Mesh generation and description	6
4.3	Numerical schemes	8
4.4	Discrete adjoint	9
5	Results	11
5.1	Grid convergence	11
5.1.1	GCI method	11
5.2	Grid convergence results	12
5.2.1	Close configuration	12
5.2.2	Open configuration	13
5.2.3	SST vs SA	15
5.2.4	Compressible vs incompressible	15
5.2.5	Flow visualization	16
5.3	Discrete adjoint	16
5.3.1	Open configuration	16
5.3.2	Optimized flap in the close configuration	19
5.3.3	Close configuration	21
6	Conclusions	23

1. Summary

This report presents the analysis of a DRS (Drag Reduction System) for a 2D rear wing section both in close and open configuration. Starting from a geometry freely inspired by a Formula SAE rear wing, a mesh convergence study was carried out focusing on the force coefficients of the DRS. The problem was tackled exploiting the open source CFD software SU2 to run numerical simulations, comparing compressible and incompressible solvers and different turbulence models.

Then this work dealt with the optimization of the shape of the flap in the open configuration using discrete adjoint implemented in SU2. The goal of the optimization was to minimize the drag while keeping the lift of the configuration constant.

In the end, the discrete adjoint was applied to the close configuration: a brief overview of the results is proposed to have further understanding of the optimization capabilities.

2. Problem definition

The drag reduction system is a key feature in modern race cars, especially when talking about Formula 1. This is the only movable aerodynamic surface accepted by regulations, and by far one of the most important appendices to maximize the car performance in terms of top speed.

The primary task of a DRS is related to the capability of overtaking: when the flap is opened, the reduction in drag combined with the slipstream effect of the preceding vehicle induce a determinant speed gain on the straights. The rear wing returns to its original configuration when this function is no more needed, with closed flap and maximum downforce generation.

Discrete adjoint techniques for the optimal design of aerodynamic surfaces are nowadays spreading in motorsports. Reaching in an automatic way an optimal shape for wings and other appendices is undoubtedly a great advantage in early design phase. This project shows how this objective can be achieved for a simplified 2D case. In this framework the aim is to find an optimal shape for the flap in order to minimize the drag in the open configuration, while assessing the impact of this optimized shape in the close configuration. Finally, an optimization of the flap in the close configuration will be presented. It is important to stress the fact that this goal is achieved by a purely qualitative point of view: the relative positioning of the main and the flap airfoils was not rigorous, with the analysis focusing mainly on the shape of the flap. Unfortunately, no reference solutions were available to validate properly the results.

2.1 Literature review

In the following will be proposed a short overview of the optimization problem and the discretization of the flow equations in SU2 as presented by T. Albring *et al.* in [1]. A simplified representation of the aerodynamic design chain could be seen in figure 2.1. The components of the design vector α for this project are the coordinates of the control points of the Free-Form deformation (FFD) method. According to a movement of the surface based on the current values of the design variables, a mesh deformation routine creates a new mesh X . The solver then evaluates the state variable U and the objective function J . Using this setting, the optimization problem incorporating a steady state constraint can be written as

$$\min_{\alpha} J(U(\alpha), X(\alpha)) \quad (2.1)$$

$$\text{subject to } R(U(\alpha), X(\alpha)) \quad (2.2)$$

where $R(U)$ is the discretized residual, which includes the flow residual and also residuals of other coupled models. This means that U also consists of the variables of these additional equations. This is the case of turbulent models, which is of special interest for this work: U will then consist also of turbulence-related quantities that ensure the closure of RANS equations. SU2 uses the Finite-Volume method on a vertex-based median-dual grid to discretize the compressible RANS equations and the turbulence models. Several numerical fluxes like JST, ROE, etc. are implemented and flux and slope limiters enable second-order space integration. These options will be further discussed later in treating numerical simulations set-up. An implicit Euler scheme is exploited for the time integration. This scheme leads to a system of coupled equations in the form $R(U) = 0$, whose solution process can be transformed into a fixed point equation:

$$U^{n+1} = U^n - P^{-1}(U^n)R(U^n) =: G(U^n) \quad (2.3)$$

The computational mesh is subject to change, and this aspect can be included in the optimization problem formulation 2.1-2.2 which takes this final form:

$$\min_{\alpha} J(U(\alpha), X(\alpha)) \quad (2.4)$$

$$\begin{aligned} \text{subject to } U(\alpha) &= G(U(\alpha), X(\alpha)) \\ X(\alpha) &= M(\alpha) \end{aligned} \quad (2.5)$$

where all functions will additionally depend on the mesh deformation (X) and the mesh sensitivity is included with $M(\alpha)$. The Lagrangian associated with this problem is the starting point for the derivation of the discrete adjoint equations:

$$L(\alpha, U, X\Lambda_f, \Lambda_g) = J(U, X, \alpha) + [G(U, X) - U]^T \Lambda_f + [M(\alpha) - X]^T \Lambda_g \quad (2.6)$$

with Λ_f, Λ_g being respectively the vectors of the adjoint flow variables and the adjoint geometry variables. Notice that the terms in square brackets are null by definition of the problem 2.5. Thus differentiating L with respect to the design variables α one get an expression of the sensitivity $J_{/\alpha}$:

$$\frac{dL}{d\alpha} = \frac{dJ}{d\alpha} + \left[\frac{\partial U}{\partial \alpha} \right]^T \left[\frac{\partial J^T}{\partial U} + \frac{\partial G^T}{\partial U} \Lambda_f - \Lambda_f \right] + \left[\frac{\partial X}{\partial \alpha} \right]^T \left[\frac{\partial J^T}{\partial X} + \frac{\partial G^T}{\partial X} \Lambda_f - \Lambda_g \right] + \frac{dM^T}{d\alpha} \Lambda_g \quad (2.7)$$

By pretending that the terms associated to $U_{/\alpha}^T$ and $X_{/\alpha}^T$ are zero, the discrete adjoint equations are obtained:

$$\Lambda_f = \frac{\partial J^T}{\partial U} + \frac{\partial G^T}{\partial U} \Lambda_f \quad (2.8)$$

$$\Lambda_g = \frac{\partial J^T}{\partial X} + \frac{\partial G^T}{\partial X} \Lambda_f \quad (2.9)$$

and finally the surface sensitivity reads

$$\frac{dL}{d\alpha} = \frac{dJ}{d\alpha} + \frac{dM^T}{d\alpha} \Lambda_g \quad (2.10)$$

Surface sensitivity is key in implementing the discrete adjoint, which relies generally on a gradient based optimization algorithm. SU2 implements an evoluted version of the basic Newton method, called Sequential Least Squares Programming (SLSP). Gradient based optimization normally suffers by the potential presence of local minima: the optimal solution is often retrieved as corresponding to the local minimum of the objective function which is nearest to the starting point in the gradient evaluation process.

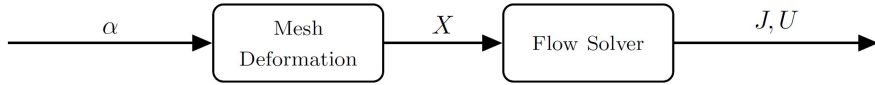


Figure 2.1: Simplified representation of the aerodynamic design chain

3. Design of Experiment

This study was developed analyzing in parallel the close and the open configuration of the DRS. The main steps are the same for both the configurations and presented below. The workflow is resumed in 3.1

1. Geometry definition: the first step consisted in the development of a DRS geometry, starting with airfoils selection and proper dimensioning.
2. Mesh generation: a suitable points progression on the airfoils was achieved to generate meshes around the DRS.
3. Numerical simulations set-up: this phase included the adjustment of several settings required by the software through the configuration file, including boundary condition, numerical solver and convergence criteria.
4. Grid convergence: mesh convergence study was required to assess the independence of the numerical results from the grid definition. This was achieved by performing three different simulations on progressively refined grids. Compressible and incompressible solvers were employed. Specifically, ROE scheme was used in the RANS case, FDS for the INC_RANS case, and different turbulence models applied (SST and SA). Results from this step were analyzed and compared.
5. Shape optimization of the flap for the open configuration: discrete adjoint methodology implemented in SU2 was exploited to minimize the drag in the open configuration on a medium mesh. Firstly, parameters for tuning the simulation were properly set to obtain good results. Then several optimizations were run by trial, observing how results changed by adjusting determined settings. This phase proceeded with a comparison between the performances of the optimized and the original open configuration, including a test of the optimized flap inserted in the closed configuration, aiming to establish the eventual loss in efficiency determined by the change in geometry.
6. Shape optimization of the flap for the close configuration: discrete adjoint methodology implemented in SU2 was applied directly to the close configuration on a medium mesh, retaining drag minimization as objective. This insight was intended to understand better how the optimization worked with a closed flap.

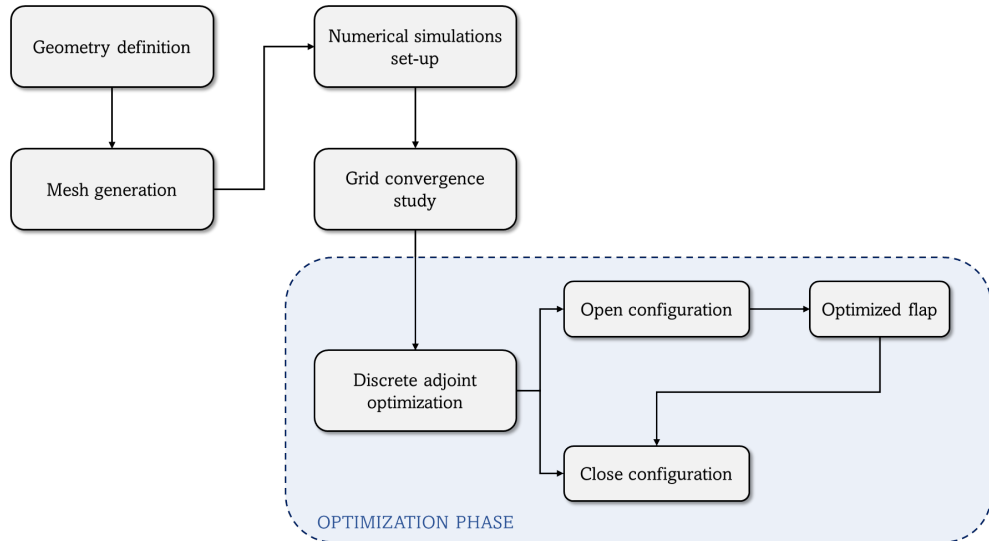


Figure 3.1: Project map

4. Computational model

4.1 Problem geometry and setup

Geometry data for this project were taken from an online airfoil database [2]. Formula SAE cars developed by the DynamisPRC team made use in last few years of FX-family profiles for rear wings, with a negative camber to produce downforce. The designated airfoil for this study was the FX 63-137, which resembled indeed a typical aerodynamic profile for a race car. A DRS device implied the presence of two airfoils: the so-called main plate, which stays fixed during all race phases, and the flap, which is the movable part of the assemble. In a closed-flap configuration, the amount of downforce produced by the rear wing is expected to be maximum (compatibly with the potentiality of the system). In an open-flap configuration, the DRS actuator rotates the flap and reduces its angle of attack, generating a gap between the main plate and the flap itself. In this way, the drag force normally generated by the rear wing is expected to drop, ensuring a big advantage in terms of speed over straights or during overtaking.

4.1.1 Geometry definition

This work focused on the 2D optimization of the system described above, so no three dimensionality is considered. No actuation system was modelled: this appendix would have been misrepresented in 2D, and it has no real importance for the purposes of this project. The main plate and flap dimension and relative position were established by looking at typical rear wing foils dimensions [3]. Table 4.1 resumes the choices for the two configurations in terms of chord (c_m, c_f), angle of attack (α_m, α_f), and leading edge position (dx, dy). In particular the open configuration was obtained by rotating the flap with respect to its trailing edge in the close configuration.

A Matlab script was elaborated to pre-process the geometry. The positioning of the appendices was carefully studied by plotting them as shown in Figure 4.1, which also reports the reference length (RL) for all simulations. The reference length was defined as the distance between the main plate LE and the flap TE, as commonly done in race car aerodynamics developing [4].

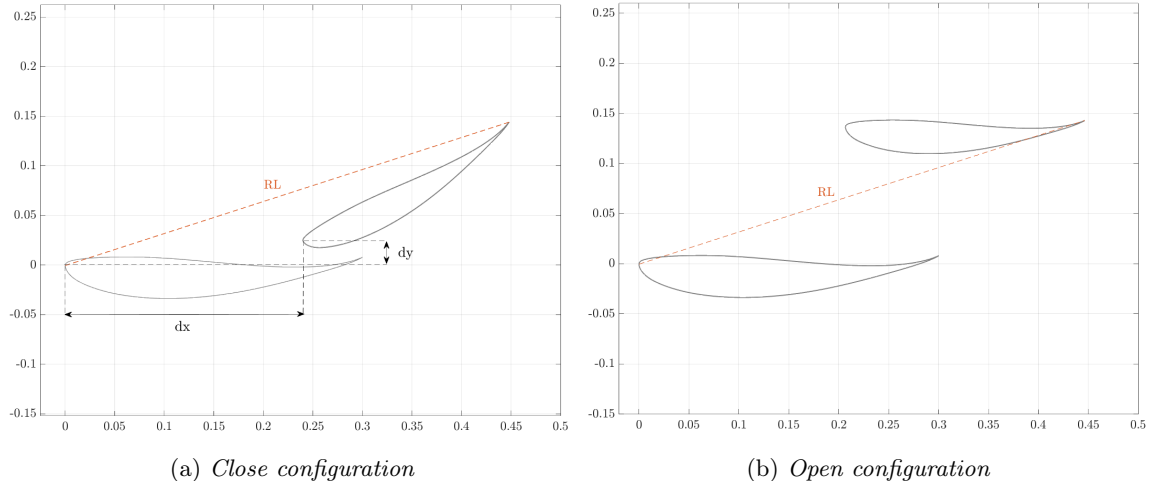


Figure 4.1: DRS geometry

RL [m]	dx [m]	dy [m]	c_m [m]	c_f [m]	α_m [°]	α_f [°], close	α_f [°], open
0.4706	0.24	0.024	0.3	0.24	-1.5°	-30°	-1.5°

Table 4.1: Geometry data

4.1.2 Boundary conditions

The Navier-Stokes adiabatic wall condition was imposed on the airfoils boundary. Specific boundary conditions for the compressible and incompressible case are distinguished below:

1. For the RANS case, compressible free stream conditions were fixed according to data reported in the table 4.2. By using a marker distinguishing the airfoils boundary and the farfield, SU2 physically retrieves the proper boundary conditions to be set.

Mach	Temperature [K]	Reynolds	α [°]
0.1	288.15	948515	0

Table 4.2: Free stream condition in RANS

2. For the INC_RANS case incompressible free stream condition were set to keep consistency with the compressible case in terms of velocity, density and viscosity. Markers were defined accordingly, and data are reported in table 4.3.

Velocity [m/s]	Density [kg/m ³]	Viscosity [m/s ²]	α [°]
34.0297	1.05978	1.7893E-5	0

Table 4.3: Free stream condition in INC_RANS

4.2 Mesh generation and description

One of the most critical issue in a numerical simulation is undoubtedly the mesh generation. A wrong choice at this stage will affect the quality of the simulations and the obtained results.

The program *gmsh* was used to generate the mesh. Given the complexity of the geometry under analysis, especially for the closed configuration, an hybrid mesh was used with an O-grid domain.

In particular, a structured grid was used near the wall of the profiles, to correctly capture the boundary layer. An unstructured mesh generated using *Delaunay* algorithm with triangular elements was used for the rest of the domain.

One of the first parameters to set was the farfield radius, from which overall mesh dimensions were determined. In general, a proper radius is important to ensure that the solution evolves unperturbed by the domain boundaries. The value was set in chords units, and a dependence of the results from this parameter will be shown in section 5.2.1. The airfoils boundary was discretized generating a set of points with optimal spacing. This was possible by developing a Matlab script which automatically set a progression of boundary points exploiting the definition of few parameters, trying to cluster points in critical areas such that the trailing edge and the leading edge. Due attention must be given also to the correct progression of the number of elements during the mesh refinement. This aspect refers to the number of elements placed onto the wall boundaries and to the total one. As estimator of the typical size of the element the following formula was used:

$$h = \frac{1}{\sqrt{N}}$$

where N is the total number of elements of the mesh.

- **Number of total elements** The main constraints on the total number of elements regarded the computational power and the correct progression, in order to perform a consistent convergence analysis. Starting from a baseline 'coarse' mesh, refined 'medium' and 'fine' meshes were generated. The number of elements for each grid was selected to maintain a constant grid refinement factor, r_{ij} , defined as:

$$r_{ij} = \frac{h_j}{h_i} = \sqrt{\frac{N_i}{N_j}}$$

The value of r_{ij} should be greater than 1.3. Letting $h_1 < h_2 < h_3$, the characteristics of the meshes are reported in 4.4 for the closed configuration and in 4.5 for the open one.

Grid	Index	N	h_i
Fine	1	193431	0.0023
Medium	2	85025	0.0035
Coarse	3	37510	0.0051

Table 4.4: Closed configuration

Grid	Index	N	h_i
Fine	1	163060	0.0025
Medium	2	72094	0.0037
Coarse	3	31865	0.0056

Table 4.5: Open configuration

- **Boundary Layer** To correctly capture the boundary layers a structured mesh was used near the wall, appropriately inserting a boundary layer field in *gmsh*. The following aspects were monitored:

1. The number of elements on the airfoils, in order to maintain a correct progression between the coarse, medium and fine mesh as shown in table 4.6 and 4.7.

Grid	Index	Elements on the main	Elements on the flap
Fine	1	558	499
Medium	2	262	231
Coarse	3	131	113

Table 4.6: Number of elements on the wall boundaries in the close configuration

Grid	Index	Elements on the main	Elements on the flap
Fine	1	585	476
Medium	2	257	211
Coarse	3	118	98

Table 4.7: Number of elements on the wall boundaries in the open configuration

2. It should be achieved a value of $y^+ \leq 1$ to have a proper discretization of the near wall region: this constraint resulted in a first cell height of 0.000002.
3. The progression of elements along the two profiles to achieve an higher elements' density at the front and rear.
4. A fan was defined in correspondence of the trailing edge. This avoided an excessive distortion of the elements and helped to better capture the flow behaviour in such a critical zone of the mesh.

- **Refinement boxes** To ensure a smooth transition between the elements of the structured and unstructured grid the refinement box field of *gmsh* was used. The method followed consisted in arranging a series of refinement boxes one inside the other. In this case the area closer to the two profiles is very dense and a smooth progression between the internal and the far field elements was obtained.

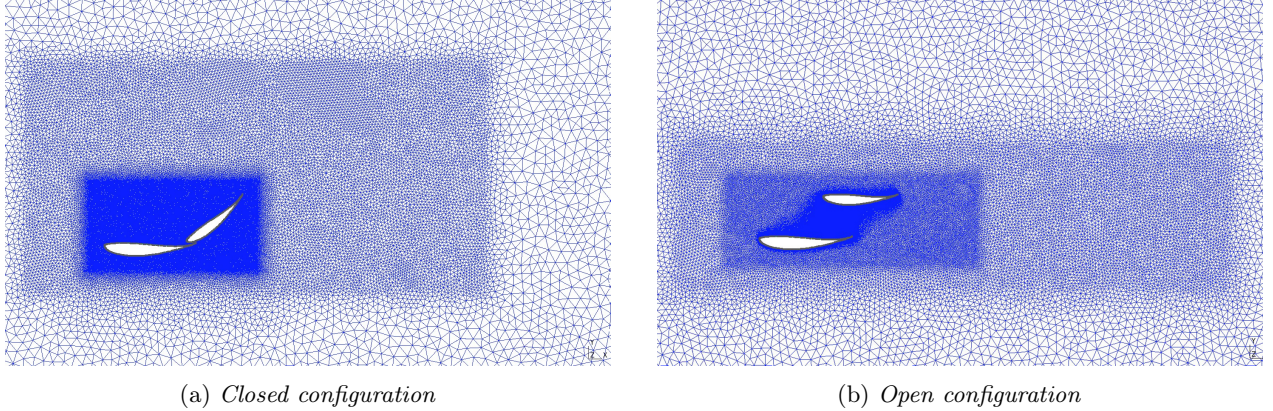


Figure 4.2: Detail of the refinement boxes

The two profiles in the close configuration were very close to each other, so that a particular attention to the area between the two was needed in order to capture the right behaviour of the flow. A detail of the mesh in that area can be seen in figure 4.3

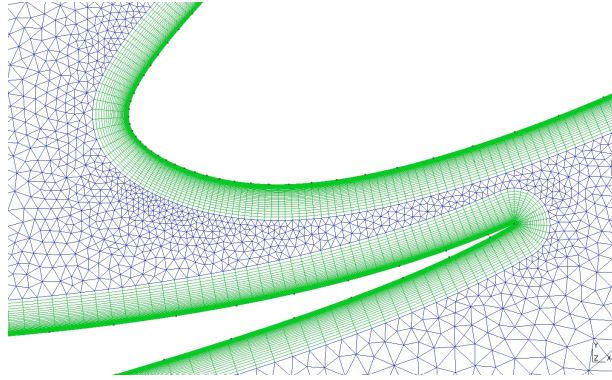


Figure 4.3: Detail of the mesh in the gap between the main and the flap

4.3 Numerical schemes

The same settings were used both for the closed and the open configuration.

Compressible (RANS) and incompressible (INC_RANS) numerical simulations were run in SU2, for which different turbulence models were applied (SA and SST).

Reference non-dimensionalization of the equations was considered by expliciting this option in the configuration file, REF_DIMENSIONALIZATION=FREESTREAM_VEL_EQ_ONE. Using this option the reference pressure is chosen such that the non-dimensional free-stream velocity equals 1.0 [7].

For the compressible case, ROE scheme was used to discretize and solve convective fluxes. Applying MUSCL scheme for fluxes reconstruction allowed to obtain second order accuracy for the numerical method, with gradients evaluation performed through the Green-Gauss theorem. Gradients were limited with VENKATAKRISHNAN slope limiter, avoiding spurious oscillations in the solution. The Venka's slope limiter coefficient ϵ is

specified with this relation:

$$\epsilon^2 = (K\Delta)^3 \quad (4.1)$$

where K is a threshold parameter and Δ is the average grid size.

The threshold parameter K should be maintained fixed to include the effects of a different average grid size for the three grids. While K is set as an input in SU2, Δ is hard-coded to 1.0. This required an adjustment to the value of the slope limiter to avoid using higher order numerical method more on coarser grids [5]. In order to maintain K fixed passing from one grid to another, the slope limiter was set to 0.075 for the finest grid, and multiplied by r_{ij} passing to coarser grids.

Grid	Refinement factor, r_{ij}	VENKAT_SLOPE_LIMITER
Fine	-	0.075
Medium	1.5083	0.075 · 1.5083
Coarse	2.2709	0.075 · 2.2709

Table 4.8: Venkatakrishnan coefficients, close configuration

Grid	Refinement factor, r_{ij}	VENKAT_SLOPE_LIMITER
Fine	-	0.075
Medium	1.504	0.075 · 1.504
Coarse	2.262	0.075 · 2.262

Table 4.9: Venkatakrishnan coefficients, open configuration

Moreover, an adaptive CFL_NUMBER was used. The Sutherland model was exploited to compute the viscosity starting from the temperature.

Since the Mach number was really low, simulations with the incompressible solver were carried out to compare results, and an upwind Flux Difference Splitting (FDS) numerical scheme with a constant viscosity model was employed, as ROE is not implemented in SU2 for the incompressible RANS. Other settings were maintained unvaried with respect to the compressible case.

As convergence criteria the residual for both the c_L and the c_D was set to 10^{-6} .

4.4 Discrete adjoint

In the discrete adjoint framework, simulations were carried out on the medium grid using a compressible RANS solver with the SST turbulent model. The aim of the adjoint was to minimize the drag while keeping constant the lift. Indeed the objective function was targeted to be the drag, and the FIXED_CL_MODE was used in order to keep the value of the c_L constant. During the direct simulation the angle of attack of the flap was updated every 250 iterations to ensure that a constant lift coefficient was maintained.

Several adjustments were introduced in the configuration file, aiming to reach convergence in a reduced number of iterations and to have a reasonable simulation time. In particular, JST was used as convective scheme, setting the second order coefficient to zero and the fourth order to 0.04 in both the direct and the adjoint simulation. JST was more stable and converged faster compared to ROE. JST also allowed to set a higher value of the CFL number, that was key to obtain faster convergence: the minimum value was increased to 50. As linear solver BCGSTAB was used with ILU as preconditioner, that is proven to work well with high values of CFL[7]. These improvements enabled to get convergence in nearly 6000 iterations.

Before running the simulation with SU2, a box enclosing the flap was created by specifying dedicated settings in the configuration file. This box was then split in sub-boxes as set in the FFD_DEGREE option. In correspondence of each vertex of the sub-box an FFD control point was placed to control the deformation of the flap. Different numbers of FFD control points were used: a comparison of the results will be shown in section 5.3.1. Mesh deformation was carried out by means of the inverse volume method.

A critical aspect regarded the setting of some important configuration options for the discrete adjoint:

- FROZEN_VISC_DISC: allows to freeze the turbulent viscosity in the discrete adjoint formulation. This is obviously a simplification that is sometimes useful to have a more stable adjoint. Optimizations were carried out with this hypothesis both activated and deactivated, with consequent results comparison.
- OPT_RELAX_FACTOR: this value was adjusted to have a deformation of the flap of the order of the millimeters, which was monitored through the log.Deform files (generated during the optimization process at every design) by means of the value *Max_Diff*.
- OPT_GRADIENT_FACTOR: this option ensured a gradient norm (GNORM) of the order of 10E-6 at the first iteration, proven to be the best one for the optimization process.
- CFL_REDUCTION_ADJFLOW: multiplication factor for the CFL in the adjoint problem with respect to the CFL in the direct problem. Theoretically it should be kept less than one, as the adjoint simulation is less stable than the direct one especially at the beginning. Practically it is better to set a value greater than one so that the first unstable iterations are overcame faster.
- RELAXATION_FACTOR_ADJOINT: a value less than one is desirable in order to smooth out high order oscillation in the adjoint simulation.

Simulations were run sticking to the procedure proposed in SU2 tutorials [7]. As first task, SU2_DEF was run to create the FFD_box enclosing the flap. Then, SU2_GEO allowed to obtain relevant geometry data. The shape optimization was launched as implemented in the Python script included in the discrete adjoint solver of SU2. It is worthwhile stressing the fact that at each successive design values of the GNORM parameter and the *Max_Diff* indication had to be controlled. Values of OPT_GRADIENT_FACTOR and OPT_RELAX_FACTOR were properly adjusted if necessary.

5. Results

5.1 Grid convergence

The grid convergence was checked following the Grid Convergence Index (GCI) method proposed by Roache [6] and explained during a curricular seminar by F.Caccia [5]. This method will be briefly described in this section, and results obtained by applying it to several simulations cases will be shown. Both closed configuration and open configuration were tested for grid convergence, yielding consistent results that showed the independence of aerodynamic coefficients values from the mesh definition. A comparison between GCI method performed using different turbulence models and solvers will be described as well.

5.1.1 GCI method

In this framework grid convergence was evaluated for two key variables, namely the global lift and drag coefficients (c_L , c_D) of the rear wing system. The whole discussion below will be held for the c_L value alone, with evident extension to the c_D case. Every simulation was run on a set of three different grids, each characterized by a different number of elements and, consequently, different average elements size, as shown in 4.2. The GCI method computes the apparent order of the numerical method, p , by solving the following system of equations by means of a fixed-point method:

$$\begin{cases} s = \text{sign}(\epsilon_{32} - \epsilon_{21}) \\ q(p) = \ln\left(\frac{r_{21}^p - s}{r_{32}^p - s}\right) \\ p = \frac{|\ln|\frac{\epsilon_{32}}{\epsilon_{21}}| + q(p)|}{\ln(r_{21})} \end{cases} \quad (5.1)$$

having previously defined these values:

$$\epsilon_{32} = c_{L3} - c_{L2}, \quad \epsilon_{21} = c_{L2} - c_{L1} \quad (5.2)$$

Richardson extrapolation is adopted to calculate an estimate of the key variable CL at zero grid spacing:

$$c_{L21,ext} = \frac{r_{21}^p c_{L2} - c_{L1}}{r_{21}^p - 1}, \quad c_{L32,ext} = \frac{r_{32}^p c_{L3} - c_{L2}}{r_{32}^p - 1} \quad (5.3)$$

The relative error and the extrapolated relative error between different grids can be defined as:

$$e_{a21} = \left| \frac{c_{L1} - c_{L2}}{c_{L1}} \right|, \quad e_{a32} = \left| \frac{c_{L2} - c_{L3}}{c_{L2}} \right| \quad (5.4)$$

$$e_{21ext} = \left| \frac{c_{L21ext} - c_{L1}}{c_{L21ext}} \right|, \quad e_{32ext} = \left| \frac{c_{L32ext} - c_{L2}}{c_{L32ext}} \right| \quad (5.5)$$

Finally, the GCI is computed with a proper safety factor $F = 1.25$ (recommended for a three-grid mesh convergence study):

$$GCI_{21} = F_S \left(\frac{e_{a21}}{r_{21}^p - 1} \right), \quad GCI_{32} = F_S \left(\frac{e_{a32}}{r_{32}^p - 1} \right) \quad (5.6)$$

Results will be shown in the next section for every simulation. The grid generation for this method was described in section 4.2.

5.2 Grid convergence results

The procedure explained in 5.1.1 was implemented in Matlab. The script includes the whole GCI method and results post-processing to obtain significant parameters and graphs resuming convergence and errors trends. Results from the GCI method will be presented in this section for a compressible solver using SST and SA (Spalart-Allmaras) turbulent model. The convergence was checked for both c_L and c_D in fully turbulent regimes by applying different turbulence models. Closed and open configurations were analysed separately with the very same approach. The solution was verified to be in the asymptotic range of convergence by verifying that:

$$g = \frac{GCI_{32}}{r^p GCI_{21}} \sim 1 \quad (5.7)$$

Aerodynamic coefficients values for the three grids are plotted and compared with the extrapolated values; moreover, percentage relative errors trends were found. The grid convergence showed satisfying results for all the tested configurations as shown in the following sections.

5.2.1 Close configuration

Both aerodynamic coefficients were considered for grid convergence. Results are reported in figures 5.1 and 5.2, including relative errors between successive grids.

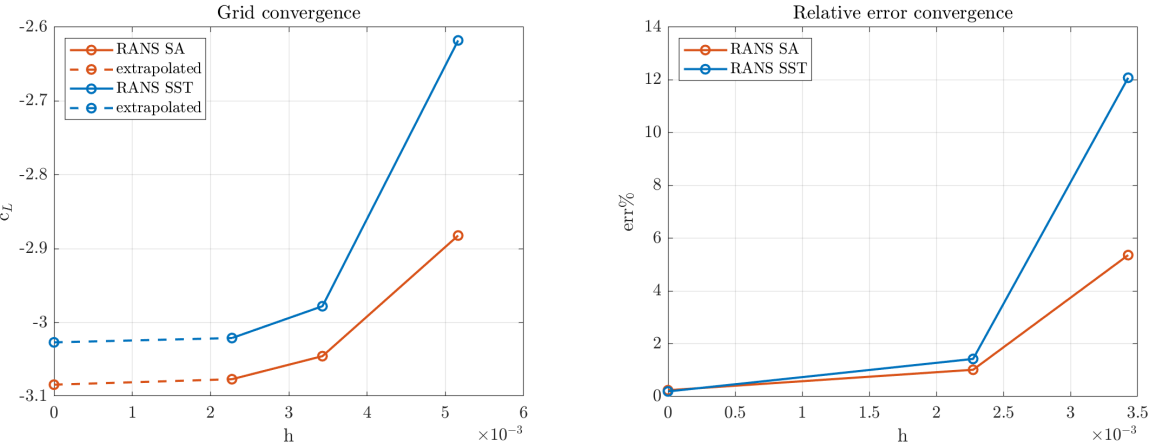


Figure 5.1: c_L convergence study, close configuration

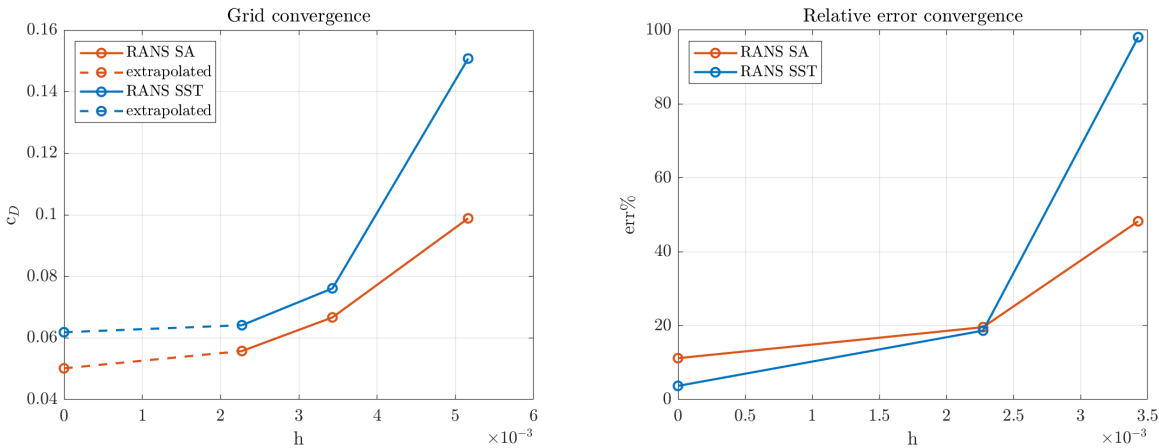


Figure 5.2: c_D convergence study, close configuration

Farfield radius dependence was tested, for the medium grid, by running several simulations changing the farfield radius in chords units. Results are shown in figure 5.3. It can be noticed that the relative error between grids with different radius is very small and converging for increasing radius confirming a good independence from this parameter. Since differences in results were not highly relevant, the radius was set to 50 chords for all the simulations. Finally, the c_p plot both for the main and the flap was retrieved based on data from surface_flow.vtu files. Results are reported below in figure 5.4. The value of g (as defined in 5.7) was near one for mostly all convergence tests, with higher deviations in the drag coefficient case. As an example, the g value in the RANS case using SST model was 1.0139 for the c_L , 0.8120 for the c_D .

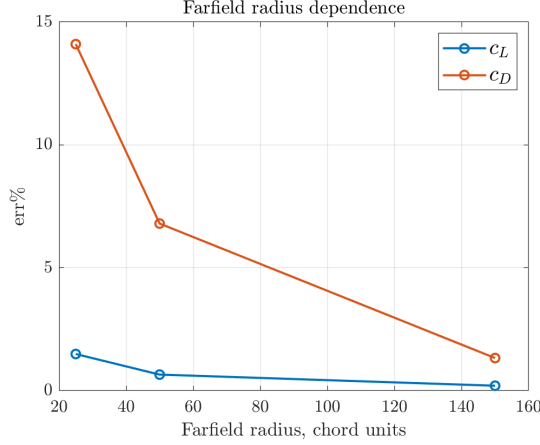


Figure 5.3: Farfield radius dependence study

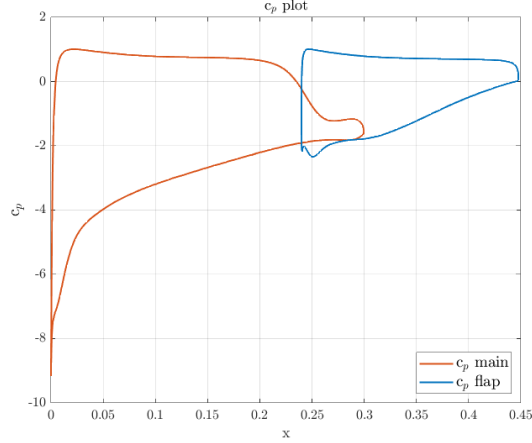


Figure 5.4: Plot of the pressure coefficient, close configuration

The value of g (as defined in 5.7) was near one for mostly all convergence tests, with higher deviations in the drag coefficient case. As an example, the g value in the RANS case using SST model was 1.0139 for the c_L , 0.8120 for the c_D .

5.2.2 Open configuration

No relevant changes in the procedure were accounted for the open configuration. A parallel grid convergence study was performed, by retaining same considerations of the previous section. Results are reported below concerning the aerodynamic coefficients convergence, relative errors (figures 5.5 and 5.6) and c_p plot (figure 5.7). As expected, the area of the c_p plot is decreased for the open configuration with an evidently smaller c_L

compared to the close configuration. The g value obtained in the RANS case using the SST turbulence model was 1.0046 for the c_L , 0.9327 for the c_D .

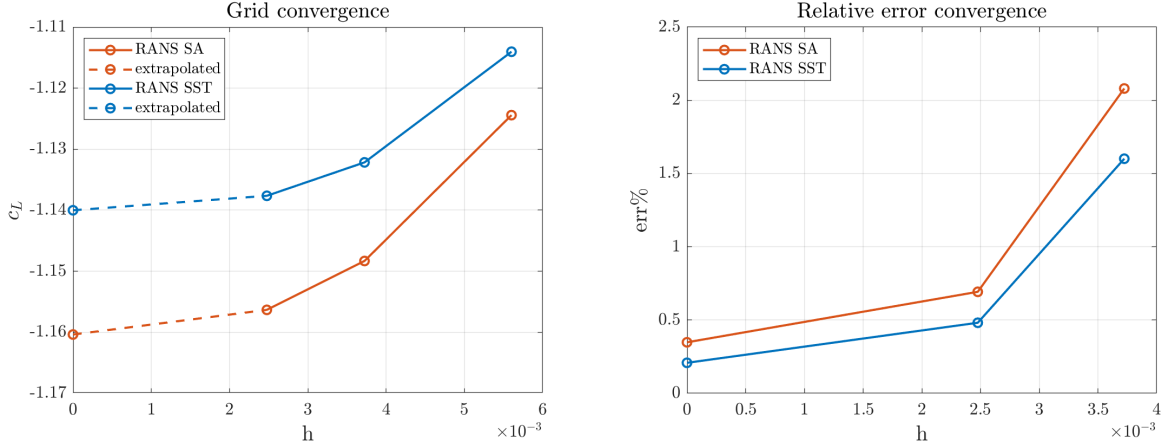


Figure 5.5: c_L convergence study, open configuration

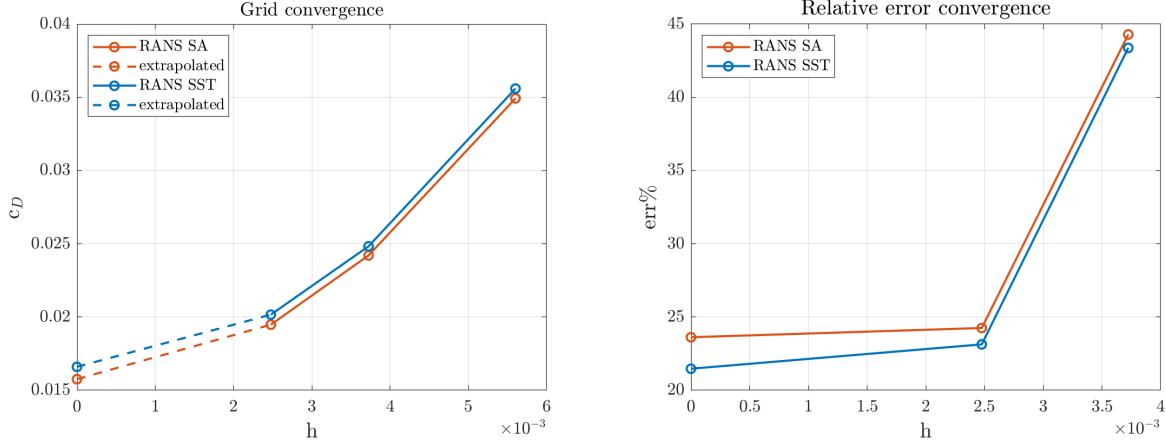


Figure 5.6: c_D convergence study, open configuration

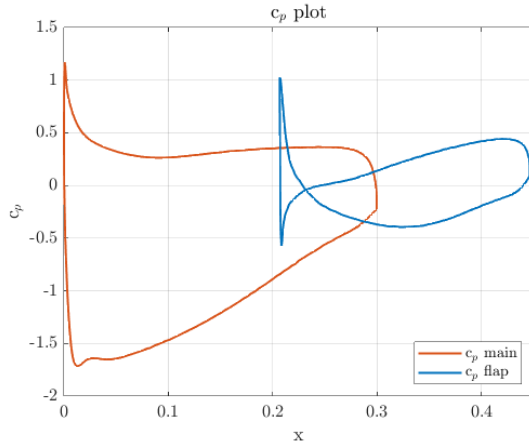


Figure 5.7: Plot of the pressure coefficient, open configuration

5.2.3 SST vs SA

Concerning the turbulence models comparison, the results were in accordance, with no evident discrepancy. They are presented in the above figures in sections 5.2.1 and 5.2.2 both for the closed and open configuration. It is possible to notice that the grid convergence is obtained also for the SA model, although the relative errors using SST are lower.

Given that SST is a 2-equation model for turbulence it is expected to behave better than the 1-equation SA, especially in the near wall region. Correction for the SA model are available, although not considered here. Since both models behaved well, the one giving lower relative errors in studying grid convergence was selected for the subsequent phases of this project. No great impact of this choice on the computational time was observed.

5.2.4 Compressible vs incompressible

As expected, given the low Mach number, the results between the RANS simulations and the INC_RANS simulations were very similar both for the closed and open configuration. In figures 5.8 and 5.9 it is shown the convergence behaviour of the incompressible simulations compared to the compressible one for the different configurations. Convergence is obtained also for the incompressible solver. In the discrete adjoint implementation of SU2 the FIXED_CL_MODE for the incompressible solver is not present, so the compressible one was used.

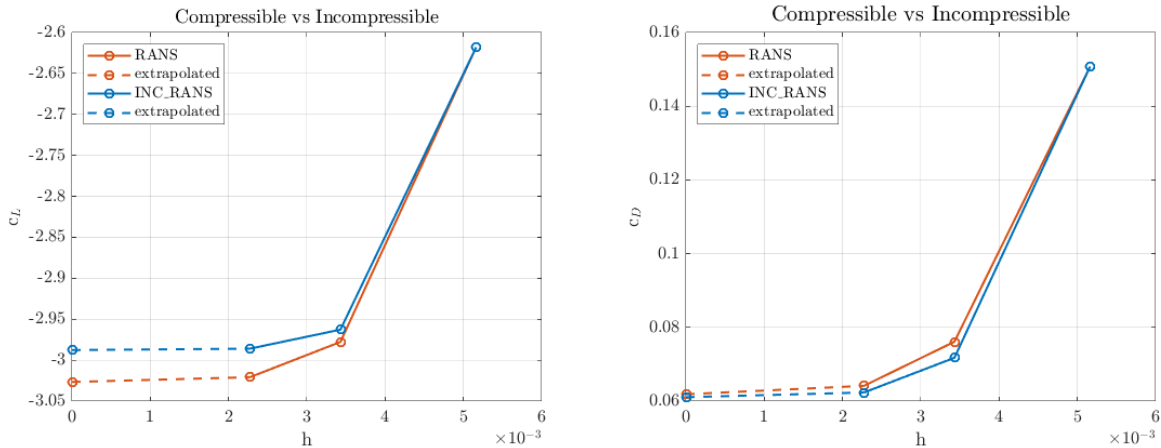


Figure 5.8: Compressible vs Incompressible, close configuration

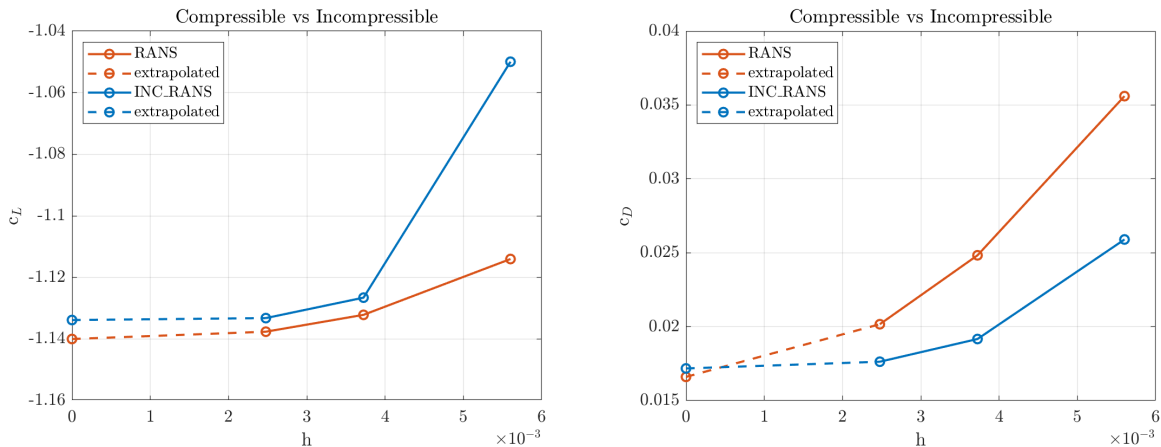


Figure 5.9: Compressible vs Incompressible, open configuration

5.2.5 Flow visualization

For the sake of completeness, in figure 5.10 are reported the visualizations of the momentum magnitude for the open and close configuration obtained during grid convergence studies using RANS with SST turbulence model.

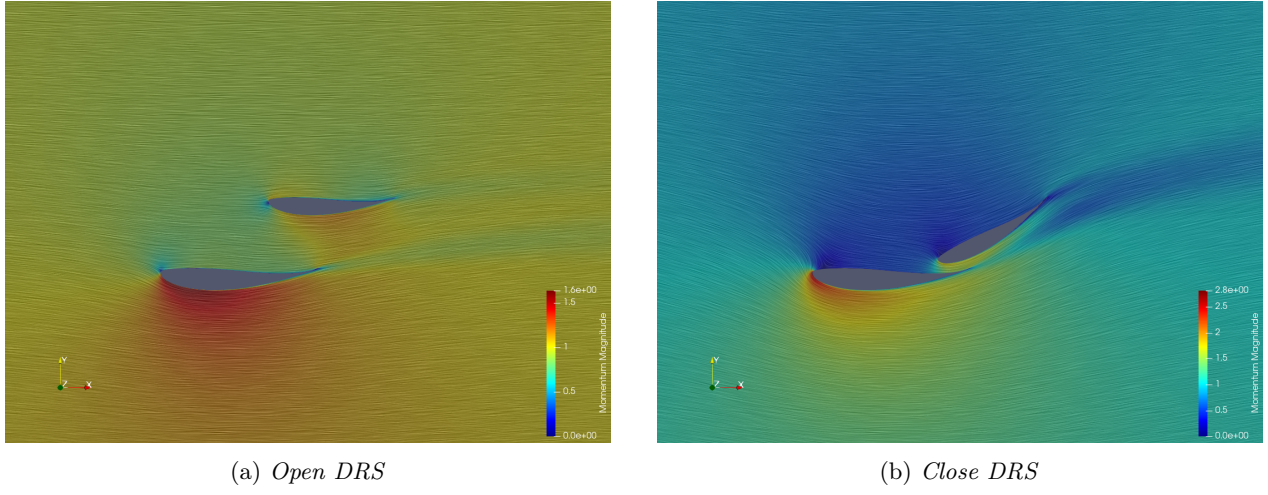


Figure 5.10: Surface LIC visualizations

5.3 Discrete adjoint

The aim of the optimization using the discrete adjoint was to find an optimized shape for the flap, while keeping the shape of the main fixed. The analyses were conducted in order to reduce as much as possible the c_D while the c_L was fixed.

The relative movement of the flap with respect to the main is obtained by an actuator, that allow to switch from open configuration to the close one. For this reason the optimization has been carried out by maintaining the flap area almost constant so that the actuator could be positioned into the flap.

Initially the value of the area of the flap was directly constrained to be above a certain threshold, that was set to be a bit less than the initial area of the flap. This was proven not to be a good constraint, since the optimization was very weak. Better results were obtained by constraining the maximum thickness of the airfoil both in terms of drag reduction and area, which was only slightly decreased during the optimization.

5.3.1 Open configuration

Geometrical data about the flap before and after the optimization are reported in tables 5.1 and 5.2, with also the values of global c_L and c_D . Firstly, the best results in terms of drag reduction are presented. These were obtained using 14 control points and the options of the optimization presented in table 5.3.

Area [m ²]	Thickness [m]	LE radius [m]	α [°]	c_D	c_L
0.00479	0.0328	218.532	-1.72°	0.021255	-1.15000

Table 5.1: Data of the flap and force coefficients before optimization, open configuration

The value of the c_D was reduced by 1.8% with respect to the original configuration, while the c_L remained constant, thanks also to a small change in the angle of attack performed by SU2. The leading edge radius angle was observed to change a lot at the end of the optimization.

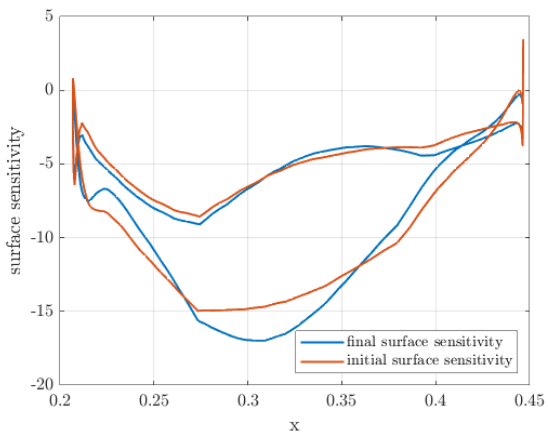
Another important aspect to be analysed was the surface sensitivity, showed in figure 5.11.

Area [m ²]	Thickness [m]	LE radius [m]	α [°]	c_D	c_L
0.00467	0.0325	283.941	-2.72°	0.02087	-1.15000

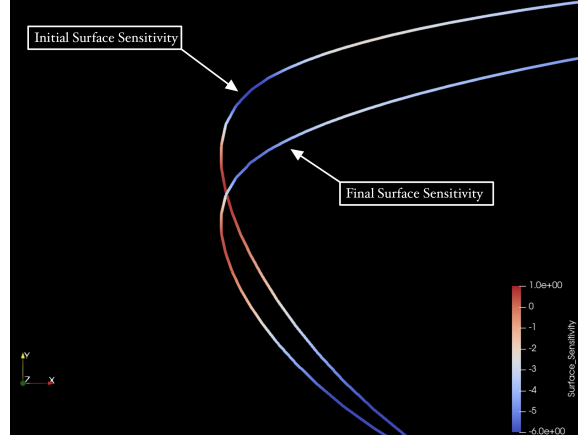
Table 5.2: Data of the flap and force coefficients after optimization, open configuration

OPT_OBJECTIVE	DRAG
OPT_CONSTRAINT	(AIRFOIL_THICKNESS > 0.03)*0.5
OPT_GRADIENT_FACTOR	1E-4
OPT_RELAX_FACTOR	1E3
RELAXATION_FACTOR_ADJOINT	1.0
CFL_REDUCTION_ADJFLOW	1.2
FROZEN_VISC_DISC	NO

Table 5.3: Configuration options of the discrete adjoint



(a) Surface sensitivity



(b) Detail of the leading edge

Figure 5.11: Surface sensitivity on the flap, open configuration

This parameter highlights the regions on the flap surface which influence mostly the objective function. The sensitivity was found to be negative almost everywhere confirming the fact that the adjoint optimizer tried to reduce the flap thickness. With respect to the initial shape, the surface sensitivity showed a decrease which is indeed symptom of a successful optimization. The only exception was represented by the bottom center region, where the sensitivity increased in module. This could be explained considering the constraint on the thickness and on the c_L : the flap was rotated to maintain the downforce fixed, therefore the lower part was expected to move downward. A detail of the surface sensitivity contour on the leading edge is reported in figure 5.11b. A comparison between the original and the optimized flap shape is proposed in figure 5.12.

The mass flux through the gap between the two airfoils, for the optimized geometry, was higher than the initial one. This aspect confirmed partially that, given the disposition of the DRS system components, the solver was modifying the shape as to let more air pass with the flap opened, which is directly related to a drag decrease. It was tricky to notice this effect by means of flow visualizations only, thus the x-momentum component (non-dimensional) was extracted in correspondence of the gap and integrated, confirming a slight increase of flux for the optimized configuration from 0.1048 to 0.1051.

In figure 5.13 is reported a comparison of the open configuration c_p distribution with the optimized and original

flap.

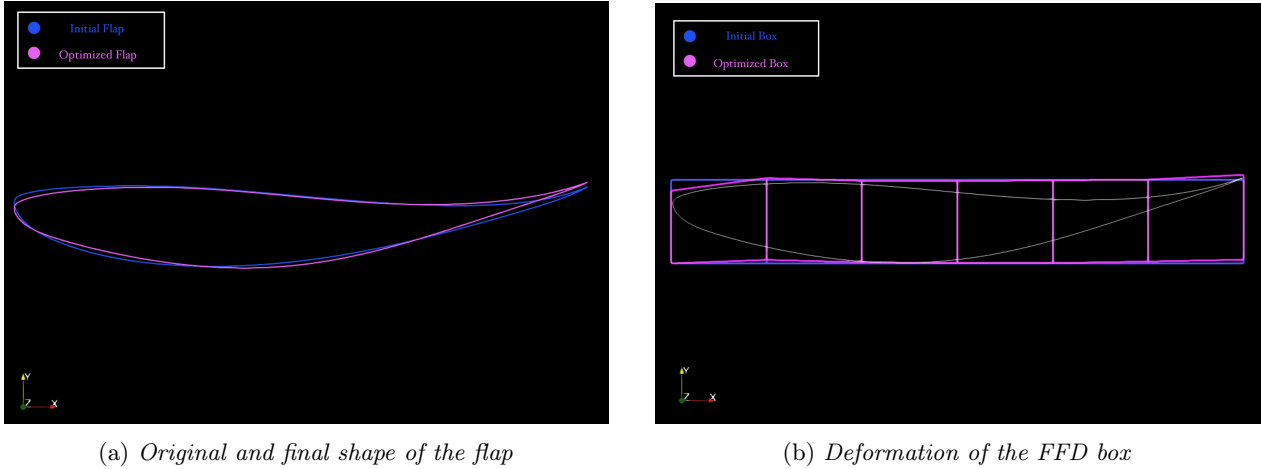


Figure 5.12: Final geometry after the optimization, open configuration

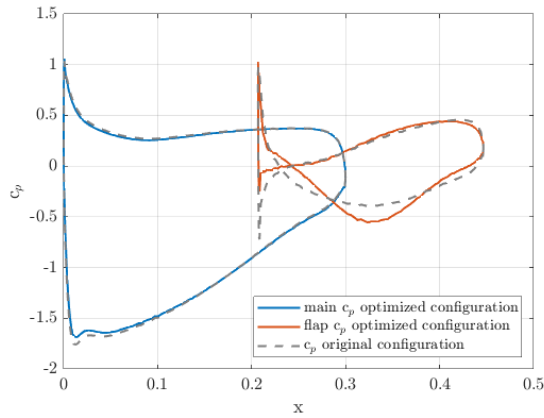


Figure 5.13: Pressure coefficient distributions, open configuration

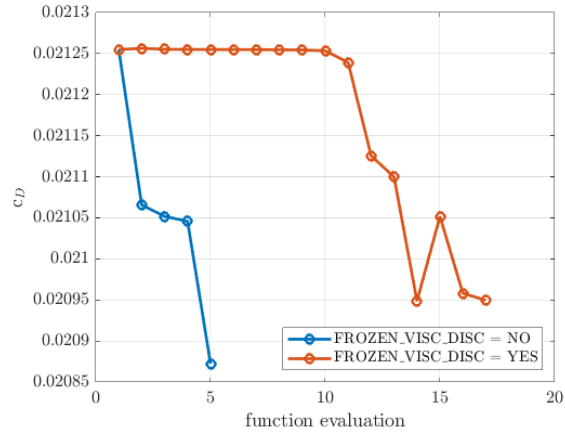


Figure 5.14: Effect of frozen viscosity hypothesis on subsequent c_D evaluations

In 5.14 the value of the drag at each iteration of the optimization process is shown, both for the case of FROZEN_VISC_DISC activated or not. A decreasing trend can be observed.

The case with FROZEN_VISC_DISC= NO performed better. In this context the turbulent field tends to highly affect the drag coefficient, and a frozen viscosity for the discrete adjoint formulation might result in a worse estimation of the c_D .

The problem was analysed also using different number of control points, trying to find the optimal number of control point in the optimization problem. The results obtained in terms of final c_D are shown in Figure 5.15. The best result was achieved using 14 control points. Using less control points did not allow a sufficient control on the deformation of the flap, while more control points led to an excessively stiff optimization problem.

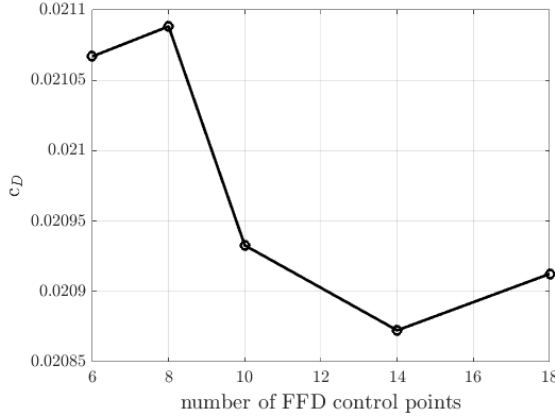


Figure 5.15: Results using different number of control points

5.3.2 Optimized flap in the close configuration

The optimized shape of the flap obtained through the discrete adjoint applied to the open configuration was tested also in the closed one. This was done in order to assess the eventual loss in downforce caused by the geometry changes, and optimal results were not expected, being the flap optimized for drag reduction while opened. To compare directly the outcomes with the original close configuration, tested during grid convergence (see 5.1.1), the same numerical scheme (ROE) and configurations were used.

It was found that the optimized flap in the closed configuration was working worse than the original one. The value of CL decreases in absolute value while the value of CD increases, as shown in table 5.4.

original c_L	original c_D	optimized c_L	optimized c_D
-2.97778	0.07611	-2.87345	0.07766

Table 5.4: Force coefficient with and without the optimized flap, close configuration

Analysing the outcome of the simulation it is possible to understand the cause of this loss of performances. The mass flux between the two profiles is increased compared to the original configuration from 0.0287 to 0.0317. In figure 5.16 it is shown the distribution of x-momentum along y, to be integrated to retrieve the mass flux, between the gap of the two airfoils at a position $x = 0.27$.

This in principle could be an improvement, being the flap not able to process that amount of air. A big recirculating bubble, that was much smaller in the original close configuration, appears near the trailing edge of the flap. Here the flow could not stay attached since in that region the optimized flap is too thin.

The presence of the recirculating bubble can be seen clearly in figure 5.17 where the streamlines labeled with the X-momentum component are put into evidence in that region. Also analyzing the skin friction coefficient, in figure 5.18a, it can be appreciated how it keeps negative values in a wider region for the optimized flap configuration, highlighting the presence of a larger recirculating region of the flow.

Finally in figure 5.18b is reported the new c_p plot of the close configuration using the optimized flap.

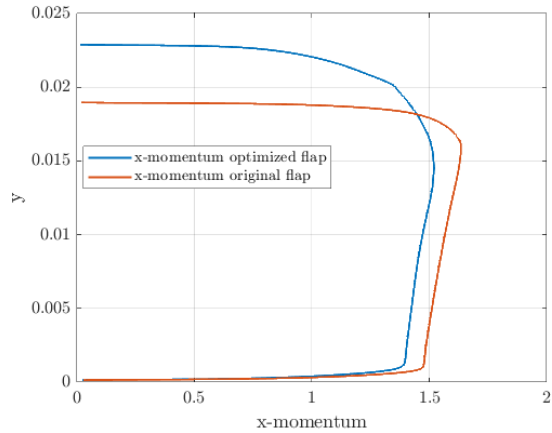


Figure 5.16: distribution of x-momentum in the gap along y

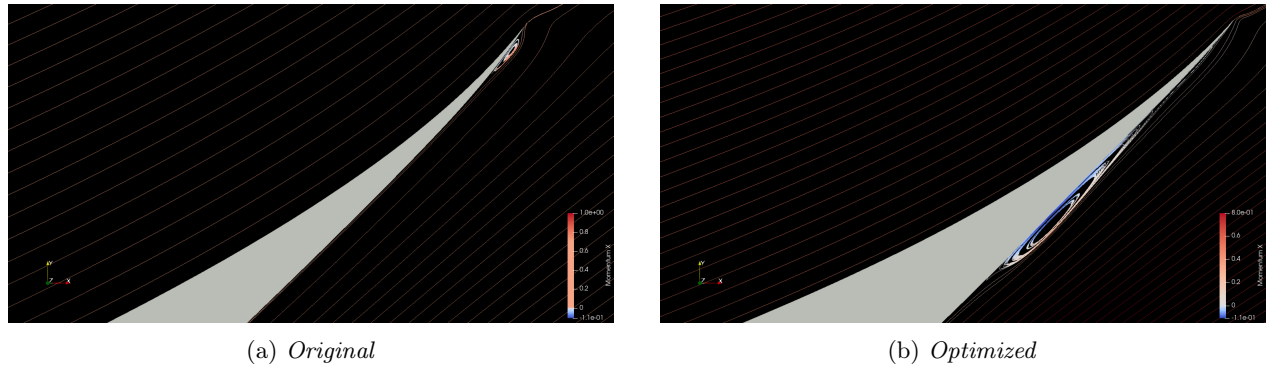


Figure 5.17: Recirculating bubble with the optimized flap

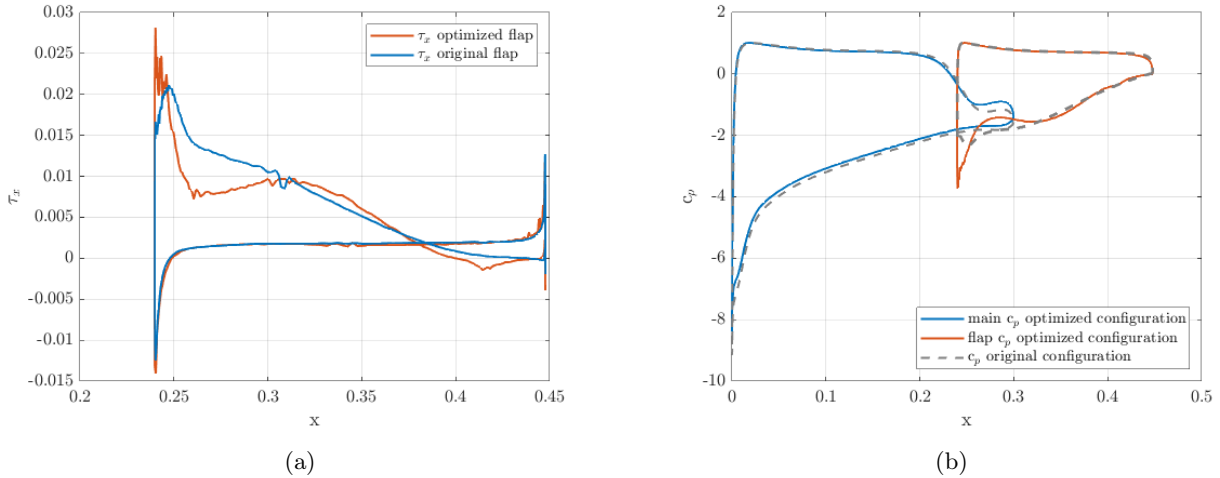


Figure 5.18: (a) Skin friction distribution on the flap; (b) Pressure coefficient distributions, close configuration

5.3.3 Close configuration

Geometrical data about the flap before and after the optimization are reported in tables 5.5 and 5.2, including the values of global c_L and c_D . This time the optimization was carried out using 10 FFD control points, with options resumed in table 5.7.

Area [m ²]	Thickness [m]	α [°]	c_D	c_L
0.00479	0.0328	-30.09°	0.06559	-3.00995

Table 5.5: Data of the flap and force coefficients before optimization, close configuration

Area [m ²]	Thickness [m]	α [°]	c_D	c_L
0.00470	0.0321	-31.34°	0.05546	-3.00986

Table 5.6: Data of the flap and force coefficients after optimization, close configuration

OPT_OBJECTIVE	DRAG
OPT_CONSTRAINT	(AIRFOIL_THICKNESS > 0.03)*0.5
OPT_GRADIENT_FACTOR	1E-6
OPT_RELAX_FACTOR	1E4
RELAXATION_FACTOR_ADJOINT	1.0
CFL_REDUCTION_ADJFLOW	1.2
FROZEN_VISC_DISC	NO

Table 5.7: Configuration options of the discrete adjoint

The value of the c_D was reduced by 15% with respect to the original configuration, while the c_L remained constant, obtaining a really good result. The value of the drag at each iteration of the optimization process is shown in 5.19a. In figure 5.19b the c_p of the close configuration with the optimized flap compared to the original configuration is reported. As it can be appreciated from the c_p plot, its distribution on the main airfoil is influenced especially in the vicinity of the trailing edge: here the c_p on the upper surface shows a less steep drop. Regarding the flap distribution, it changed mostly on the lower side, where the c_p tends to stay constant for a wider range of x .

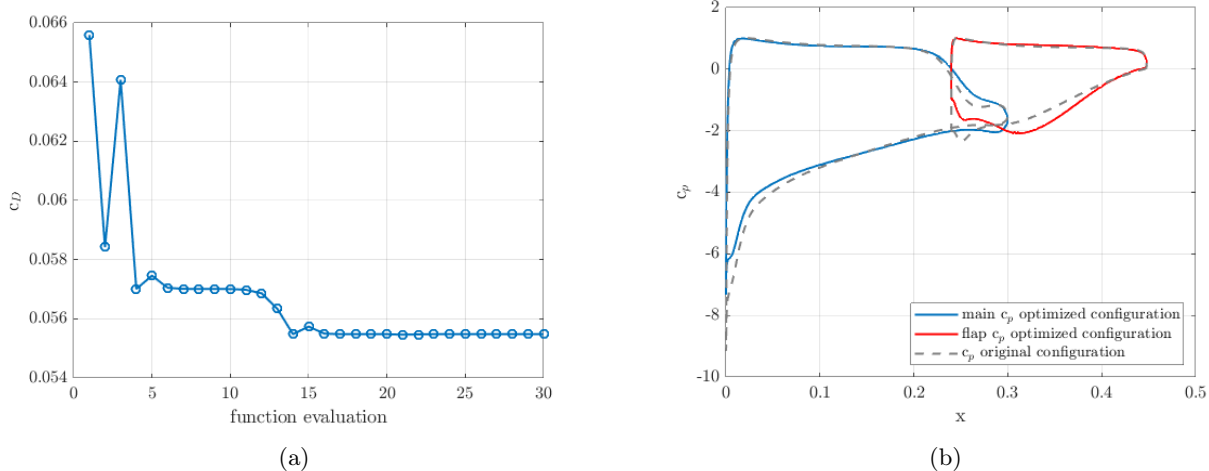


Figure 5.19: (a) c_D value at each iteration; (b) Pressure coefficient distributions, close configuration

The surface sensitivity was analysed also for this optimization: results are shown in figure 5.20. For this case similar observations can be made: the sensitivity is decreased particularly in the leading edge region. A peak in correspondence of the trailing edge is reduced after the optimization. Moreover, the top of the profile in this case highlights a marked sensitivity decrease that was absent for the open configuration. The higher drag reduction may be addressed to this aspect. A comparison between the original and the optimized flap shape is proposed in figure 5.21.

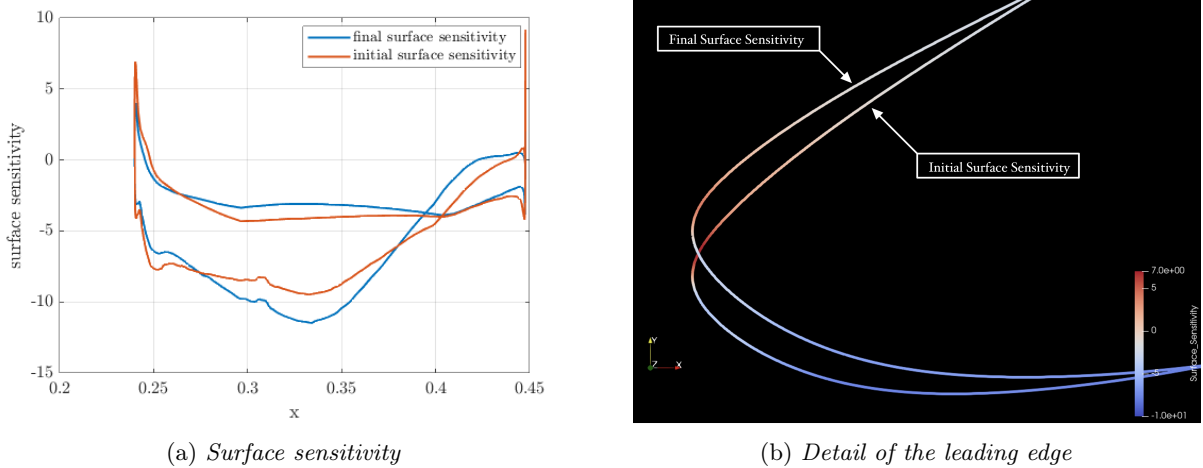


Figure 5.20: Surface sensitivity on the flap, close configuration

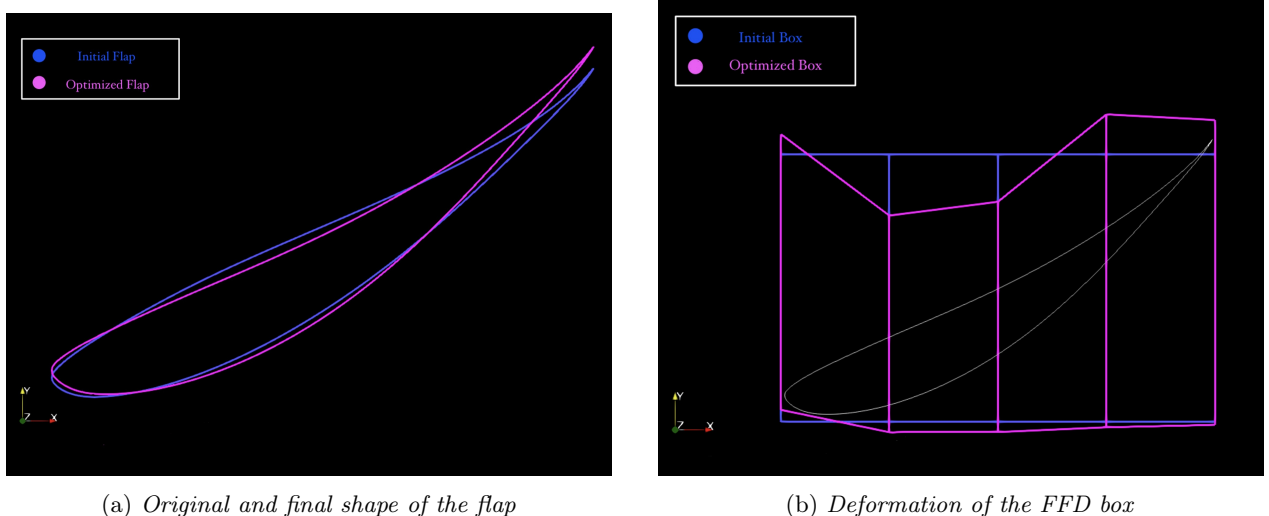


Figure 5.21: Final geometry after the optimization, close configuration

6. Conclusions

This report shown a qualitative two-dimensional analysis shape optimization for a race car airfoil. The aim of this study was primarily related to drag minimization for the open configuration, keeping an eye on the influence of the optimized design on the closed one. The geometry definition phase was intended to deliver a 2D assemble resembling a real rear wing section, with reference to typical Formula SAE data.

The consequent mesh generation included a grid convergence study, which was expected to guarantee the independence of results from the grid definition. This was verified successfully in 5.1.1. An higher sensitivity in mesh refinement was seen for the drag coefficient, which was the target of the optimization, but a further mesh refinement was not achieved due mainly to the computational cost associated to the adjoint optimization phase. Many comparisons were made including different turbulent methods and the implementation of an incompressible solver, with no great influence on results. In the latter case, the choice of a very low Mach number indicated clearly that a small effect of compressibility was expected.

The discrete adjoint optimization was run choosing a medium mesh. The shape of the flap was modified to reduce the drag, by fixing the lift coefficient and trying not to reduce much the airfoil area. In the open configuration case, the c_D was lowered by 1.8%. The optimized flap from this phase was also tested in the closed configuration to assess its performances. It would have been desirable to have a new shape which left the downforce unvaried: unfortunately, the c_L decreased in absolute value while the c_D increased. Therefore a gain in terms of drag in the open configuration was not confirmed in the closed one, which revealed a worsening in efficiency with respect to the initial geometry.

Further developments in these terms could investigate an adjoint optimization for the lift coefficient, being able to find the optimal compromise between the two operating conditions (close vs open flap).

Lastly, the flap in the close configuration was directly optimized for drag. This allowed to highlight the potentiality of the optimization for the close DRS obtaining much better results in terms of drag reduction (15%) while preserving the downforce.

Bibliography

- [1] **T. Albring et al.**: «Efficient Aerodynamic Design using the Discrete Adjoint Method in SU2», 17th AIAA/ISSMO Multidisciplinary Analysis and Optimization Conference (2015)
- [2] **UIUC Airfoil Data Site**, https://m-selig.ae.illinois.edu/ads/coord_database.html
- [3] **M. Fozan Ur Rab et al.**: «Comparative analysis of high-lift airfoils for motorsports applications», Department of Mechanical Engineering, NED University of Engineering & Technology, Pakistan (2018)
- [4] **J. Katz**: «Race car aerodynamics», Bentley publishers (1995)
- [5] **F. Caccia**: «Clean airfoil aerodynamics»
- [6] **I. B. Celik et al.**: «Procedure for estimation and reporting of uncertainty due to discretization in CFD applications», Journal of fluids Engineering - Transactions of the ASME 130.7 (2008).
- [7] **The SU2 Official Website**,
https://su2code.github.io/tutorials/Inviscid_3D_Constrained_ONERAM6/
https://su2code.github.io/tutorials/Turbulent_2D_Constrained_RAE2822/
https://su2code.github.io/docs_v7/Physical-Definition/initial-state-and-non-dimensionalization
- [8] **Compute Grid Spacing for a Given Y+**, Pointwise Inc., <https://www.pointwise.com/yplus/index.html>
- [9] **R. J. LeVeque**: «Numerical methods for conservation laws», ETH Zürich, Birkhäuser (1992)

Resources

GitHub repository including relevant files (configuration files, Matlab scripts) available at:
https://github.com/colitocoler/CFD_project.git